Biochimica et Biophysica Acta, 1056 (1991) 301–315

ADONIS 000527289100073R

BBABIO 43336

On the mechanism of the primary charge separation in bacterial photosynthesis

M. Bixon [1], Joshua Jortner [1] and M.E. Michel-Beyerle [2]

[1] *School of Chemistry, Raymond and Beverly Sackler Faculty of Exact Sciences, Tel-Aviv University, Tel-Aviv (Israel)* and [2] *Institut für Physikalische und Theoretische Chemie, Technische Universität München, Garching (F.R.G.)*

(Received 20 March 1990)
(Revised manuscript received 28 August 1990)

Key words: Photosynthesis; Reaction center; Electron transfer; Parallel sequential-superexchange mechanism; (Bacteria)

In the light of recent experimental work on femtosecond electron transfer kinetics in the reaction center (RC) we explore the mechanism for the primary process. We focus on the special role of the bacteriochlorophyll monomer (B) located between the primary donor ($^1P^*$), a bacteriochlorophyll dimer (P), and a bacteriopheophytin (H), considering a kinetic scheme which combines two parallel pathways of electron transfer: a unistep superexchange channel mediated via electronic interactions with P^+B^-H, and a two-step sequential channel involving a P^+B^-H chemical intermediate. In this kinetic scheme we used microscopic nonadiabatic electron transfer rates, which were extended to incorporate the effects of medium-controlled dynamics. The results of the kinetic modelling are presented as a function of the free-energy gap ΔG_1 between the equilibrium nuclear configurations of the donor $^1P^*BH$ and the (physically and/or chemically) mediating state P^+B^-H. The parallel sequential-superexchange mechanism reduces to the limit of nearly pure sequential pathway for large negative ΔG_1 at all temperatures and to the limit of almost pure superexchange pathway for large positive ΔG_1 at all temperatures and for moderate ΔG_1 at low temperatures. The existing femtosecond kinetic data at room temperature are consistent with either the superposition of sequential and superexchange at all temperatures or to a superposition of superexchange and sequential at room temperature and superexchange at low temperatures. The available femtosecond data at 10 K raise the possibility that the mechanism involves the superposition of superexchange and sequential at 300 K and the dominance of superexchange at low temperatures. Auxiliary experimental information regarding magnetic data, i.e., the singlet-triplet splitting of the radical pair P^+BH^-, the kinetics of the charge separation in mutagenetically altered RCs, with tyrosine M208 being replaced by phenylalanine, and the unidirectionality of charge separation across the A branch of the RC are analysed in terms of the proposed mechanism. The prevalence of the parallel sequential and superexchange electron transfer routes for the primary charge separation would introduce an element of redundancy, which insures the occurrence of an efficient process which is stable with respect to the variation energetic parameters in different photosynthetic RCs.

I. Introduction

The primary charge separation in photosynthesis constitutes a central energy conversion process in biology. Extensive experimental information has been accumulated regarding the primary charge separation in bacterial photosynthetic reaction centres (RC), which involves direct femtosecond spectroscopic data as well as auxiliary data, e.g., the effects of external magnetic and electric fields and supplementary kinetic information. The X-ray structure analysis of the RCs of *Rhodopseudomonas viridis* [1] and *Rhodobacter sphaeroides* [2,3] shows a quasisymmetric arrangement of the prosthetic groups in two membrane-spanning branches, A and B, which are composed predominantly of two protein subunits, L and M. All the mechanisms proposed for the primary electron transfer (ET) process from the singlet excited state ($^1P^*$) of the bacteriochlorophyll dimer (P) along the A branch attribute a special role to the accessory monomer bacteriochlorophyll (B), which is located between P and a bacteriopheophytin (H). Two classes of mechanisms were advanced:

Abbreviations: RC, reaction center; P, bacteriochlorophyll dimer; B, bacteriochlorophyll; H, bacteriopheophytin; ET, electron transfer.

Correspondence: J. Jortner, School of Chemistry, Raymond and Beverly Sackler Faculty of Exact Sciences, Tel-Aviv University, 69978 Tel-Aviv, Israel.

(1) The one-step superexchange mechanism [4–16]

$$^1P^*BH \rightarrow P^+BH^- \quad (1)$$

The direct ET from $^1P^*$ to H is mediated by superexchange electronic interactions via the virtual vibronic states of P^+B^-H, which are located in energy above that of $^1P^*BH$ (Fig. 1). This mechanism involves unistep ET via 'physical mediation' by B.

(2) The two-step sequential ET [17–23], which involves a genuine chemical intermediate. Several alternatives were proposed for the chemical intermediate, e.g., P^+B^-H, with the sequential mechanism being

$$^1P^*BH \overset{k_1}{\rightarrow} P^+B^-H \overset{k_2}{\rightarrow} P^+BH^- \quad (2)$$

This mechanism involves 'chemical mediation' by P^+B^-H, which is accessible by an activated or activationless crossing of the nuclear potential energy surfaces.

The first femtosecond time-resolved absorption spectroscopy on RCs of *Rb. sphaeroides* [24] and *R. viridis* [25] performed at room temperature seemed to indicate that

(i) No intermediate involving B^- was observed, within experimental uncertainty.

(ii) No bleaching in the absorption band of B was documented.

(iii) The time-resolved spectra indicate that the decay of $^1P^*$ and the build-up of P^+BH^- are characterized by the same single time constant.

These conclusions seemed to be strongly supported by the corresponding measurements at 10 K [26]. These results are consistent with a unistep superexchange mechanism, although a sequential mechanism with $k_2 \gg k_1$ cannot be ruled out. Furthermore, the analysis of electric field effects on the fluorescence polarization [27] indicates charge separation via a superexchange mechanism at low temperatures provided that the measurements are performed in the excitation dichroism mode [28]. However, picosecond time-resolution of the fluorescence is necessary in order to safely exclude an 'artifact' of the steady signal due to reaction centers with slow charge separation in a heterogeneous sample.

More recent femtosecond spectroscopic studies [29] shed doubt on the previous conclusions regarding the validity of the kinetic evidence for superexchange-mediated primary ET in the RC of *Rb. sphaeroides* at 300 K. The femtosecond data of Holzapfel et al. [29] were analysed in terms of a sequential electron transfer process. On the other hand, the femtosecond data of Kirmaier and Holten [30] were analysed in terms of a unistep primary electron transfer in a heterogeneous system, where the rate is dependent on the interrogation wavelength. These recent experimental data and their analysis [29,30] raise two distinct issues. First, what is the mechanism of the primary charge separation? Second, what are the effects of heterogeneity on the primary process? A scrutiny of the results of the analysis of Kirmaier and Holten (Fig. 2, Ref. 30) raises two difficulties: (i) The fit of the kinetic data in terms of two (interrogation wavelength dependent) time constants could not be accomplished in the relevant region of 765–796 nm. (ii) The common kinetic complexity for the time constraints for electron transfer to H and for the quionone reduction invoked by Kirmaier and Holten [30] does not hold in the range 805–825 nm at room temperature and does not apply over their entire interrogation wavelength region at 77 K. Thus, the effects of heterogeneity on the primary ET require further elucidation. The femtosecond spectroscopic data of Holzapfel et al. [29] for *Rb. sphaeroides* at 300 K were interpreted in terms of the following picture:

(i) The primary ET kinetics involves two time constants, $(3.5 \pm 0.4 \text{ ps})^{-1}$ and $(0.9 \pm 0.3 \text{ ps})^{-1}$.

(ii) These kinetic data are consistent with rate-determining reduction of B followed by a fast reduction of H.

Accordingly, these femtosecond results for *Rb. sphaeroides* seems to support the sequential mechanism (2) at room temperature. On the other hand, the low-temperature data for both *Rb. sphaeroides* and *Rps. viridis* seemed to be consistent with a single time constant, pointing towards the possibility of the unistep superexchange mechanism (1) at 10 K. Thus, in spite of the extensive experimental information, the mechanism of the primary charge separation in bacterial RCs is not yet understood.

The theoretical exploration of the primary charge separation in the RC rests on the conventional nonadiabatic ET theory and its possible extensions to encompass adiabatic and medium-controlled ET. The implementation of the theory requires information regarding energetic parameters, such as the energy gap between the equilibrium nuclear configuration between $^1P^*$ and P^+B^-H which, in spite of recent progress, cannot be reliably calculated. This is a serious technical limitation, which precludes any a priori theoretical mechanistic predictions regarding the primary ET. At present one has to utilize the ET theory for providing a conceptual framework and for the extraction of the microscopic electronic and nuclear parameters, which specify the ET dynamics.

The analysis of the primary charge separation in terms of one distinct mechanism, involving either the superexchange (1) or the sequential (2) ET, may be questionable, as both mechanisms can prevail in parallel. Marcus [17,22] and Bixon, Jortner and Michel-Beyerle [14,15] considered the competition between the superexchange and the sequential mechanisms to derive conditions for the dominance of superexchange channel. In a previous analysis of the superexchange mechanism we have emphasized [15] that an inevitable consequence of the unistep superexchange process is the occurrence

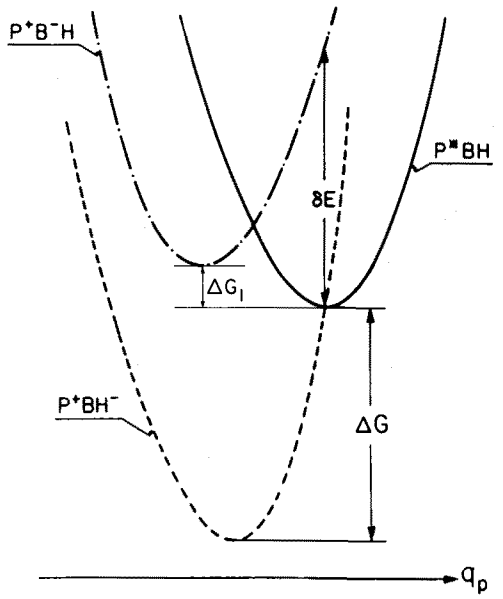

Fig. 1. Nuclear potential energy curves for the parallel sequential-superexchange mechanism. The superexchange occurs by the unistep activationless crossing from the P*BH curve (solid line) to the P^+BH^- curve (dashed line), while the first step (k_1) in the two-step sequential process occurs (in the classical limit) by thermal activation on the P*BH curve to its crossing with the P^+B^-H curve (dash-dotted line) followed by curve crossing. ΔG and ΔG_1 are the free-energy gaps between P*BH and P^+BH^- and between P*BH and P^+B^-H, respectively, while δE is the vertical energy difference.

of the parallel sequential ET process, which takes place at the intersection of the potential surfaces of $^1P^*BH$ and P^+B^-H. In Fig. 1 we portray model potential surfaces for the primary ET, which correspond to an activationless superexchange (with a rate k) and an activated sequential process (with a rate k_1). Modification of the free-energy gap, ΔG_1, between $^1P^*$ and P^+B^- and the medium reorganization energies λ and λ_1 (Fig. 1) may result in other characteristics of the rates k and k_1. One should also note in this context that a nearly activationless ET can be realized over a rather broad range of the energetic parameters, so that both k and k_1 can be nearly activationless.

In this paper we analyze the parallel sequential-superexchange kinetic scheme for the primary ET in the RC. As will be shown, this kinetic scheme is consistent with the available experimental information over a broad range of acceptable combinations of energetic parameters ranging from the purely sequential limit to a superposition of a thermally activated sequential and a superexchange mechanism. A central assumption inherent in the present analysis is that the RC is a microscopically homogeneous donor/acceptor system. Inhomogeneous broadening of energetic and nuclear parameters, which results from a continuous or multimodal distribution of the ET rates, was not considered.

II. Primary ET kinetics

II-A. Kinetic analysis

The basic kinetic scheme for the primary process (Fig. 2) includes two ET pathways: (i) a superexchange channel with a rate constant k; (ii) a sequential channel with rate constants k_1 and k_{-1} for the direct and reverse first step, respectively, and k_2 for the second step. The reverse and direct steps are related by $k_{-1} = k_1 \exp(\Delta G_1/k_BT)$, where k_B is the Boltzmann constant. The back-reaction k_{-1} can be significant at room temperature, and has to be incorporated, while the back-reactions $P^+BH^- \xrightarrow{k_-} P^*BH$ and $P^+BH^- \xrightarrow{k_{-2}} P^+B^-H$, which are characterized by large values of $\Delta G/k_BT$ (see subsection II-C) can be neglected.

The kinetic analysis of the time-dependent relative concentrations [P*BH], $[P^+B^-H]$ and $[P^+BH^-]$ is presented in Appendix A. The system is characterized by two time constants, $\tau_1 = (-s_-)^{-1}$ and $\tau_2 = (-s_+)^{-1}$, where s_+ and s_- are the solutions of Eqn. A.5,

$$s_+ = -[k + k_1 + k_{-1} + k_2 + \delta]/2$$

$$s_- = -[k + k_1 + k_{-1} + k_2 - \delta]/2 \qquad \text{(II.1)}$$

with

$$\delta = [(k + k_1 + k_{-1} + k_2)^2 - 4(kk_{-1} + kk_2 + k_1k_2)]^{1/2} \qquad \text{(II.1)}$$

From Eqns. II.1 and A.6, explicit expressions can be derived for the concentration of the P^+B^- intermediate. The maximum concentration of the intermediate P^+B^-H is obtained from the equation $d/dt[P^+B^-H](t = t_{max}) = 0$. The time t_{max} when the maximum concentration is achieved is

$$t_{max} = 1/(s_+ - s_-)\ln\left(\frac{s_-}{s_+}\right) \qquad \text{(II.3)}$$

and the maximum concentration of P^+B^-H, i.e., $B_{max} = [P^+B^-H](t = t_{max})$, is

$$B_{max} = \frac{k_1}{s_+ - s_-}\left[\left(\frac{s_-}{s_+}\right)^{\frac{s_+}{s_+ - s_-}} - \left(\frac{s_-}{s_+}\right)^{\frac{s_-}{s_+ - s_-}}\right] \qquad \text{(II.4)}$$

The fraction of reaction that proceeds through the sequential channel is given by:

$$F_{seq} = \int_0^\infty k_2[P^+B^-H](t)\,dt = \frac{k_1k_2}{s_+s_-} \qquad \text{(II.5)}$$

which provides the branching ratio between sequential and superexchange channels.

The kinetic scheme (Fig. 2) results in the following features: (i) two time constants, τ_1 and τ_2, exists, which are determined by the rates k_1, k_{-1}, k_2 and k. (ii) The

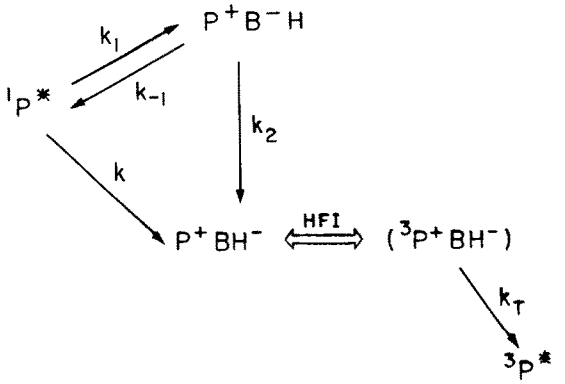

Fig. 1. A kinetic scheme for the competition between unistep superexchange at the sequenced ET routes. The formation and recombination of the $^3(P^+ BH^-)$ radical pair is also shown.

decay of [P*BH] is, in principle, biexponential with the amplitudes being determined by the rates. (iii) The time evolution of the intermediate $[P^+B^-H]$ is biexponential with equal amplitudes. (iv) In view of the temperature dependence of the rates and, in particular, of k_{-1} and also possibly of k_1, the branching ratio, F_{seq}, is expected to be temperature-dependent.

II-B. Electron transfer theory

The conventional nonadiabatic ET rate constant, k^{NA}, is given by [31,32]:

$$k^{NA} = \frac{2\pi}{\hbar} V^2 F \tag{II.6}$$

where V is the electronic coupling and F the thermally averaged nuclear Franck-Condon factor.

The electronic coupling, V, for the direct ET rates is given by $V_{PB} = \langle {}^1P^*BH | \hat{H} | P^+B^-H \rangle$ for k_1, and by $V_{BH} = \langle P^+B^-H | \hat{H} | P^+BH^- \rangle$ for k_2, where $\hat{H}$ is the Hamiltonian for the system. The superexchange interaction for the unistep rate, k, is given by

$$V_{super} = V_{PB} V_{BH} / \delta E \tag{II.7}$$

where δE is the vertical energy gap (Fig. 1).

The thermally averaged Franck-Condon factor at high temperatures is given by

$$F = (4\pi\lambda k_B T)^{-1/2} \exp[-E_a / k_B T] \tag{II.8}$$

where λ is the medium reorganization energy and E_a is the activation energy

$$E_a = (\Delta G + \lambda)^2 / 4\lambda \tag{II.9}$$

Here ΔG is the free energy gap between the equilibrium nuclear configuration of reactants and products. Eqn. II.8 corresponds to the classical limit where $k_B T > \hbar\omega_0$, where ω_0 is the characteristic frequency of the protein medium ($\omega_0 \simeq 80$–100 cm^{-1}).

The validity of the nonadiabatic ET rate rests on two assumptions:

(1) Negligible adiabatic corrections [11,22]. The process is nonadiabatic in the Landau-Zenner sense, satisfying the condition

$$\gamma_{LZ} = 2\pi V^2 / \hbar\omega_0 (2\lambda k_B T)^{1/1} < 1 \tag{II.10}$$

Setting $\gamma_{LZ} = 0.5$ as the upper limit for the nonadiabatic limit and taking $\omega_0 = 80$–100 cm^{-1} [11,15] and $\lambda = 1000$ cm^{-1}, then the nonadiabaticity condition $\gamma_{LZ} \leqslant 0.5$ at room temperature (300 K) is satisfied for $V \leqslant 70$ cm^{-1} and the maximum value for the nonadiabatic activationless rate which corresponds to $E_a = 0$ is given from Eqns. II.7 and II.8 by $k^{NA} \leqslant (250 \text{ fs})^{-1}$ at 300 K. As all experimentally recorded elementary ET rates at room temperature [24,25,29,30] are slower than this upper limit for k^{NA}, the Landau-Zenner adiabatic effects do not have to be further considered.

(2) Negligible effects of medium relaxation-excitation. The excitation and relaxation of the nuclear medium modes, which couple to the relevant electronic states, are fast on the time-scale of the electronic ET rate, thus allowing the separation of the time-scales for fast medium excitation-relaxation and slow rate-determining ET. This situation is realized when the adiabaticity parameter [33]

$$\kappa = \frac{4\pi V^2 \tau_s}{\hbar\lambda} \tag{II.11}$$

is small, i.e., $\kappa \ll 1$, where τ_s is the longitudinal medium relaxation time induced by a constant charge. The value of $\tau_s \simeq 200$ fs for the RC was inferred from molecular dynamics [34] simulations for the RC at room temperature.

Medium relaxation effects on ET dynamics are realized when $\kappa \gtrsim 1$ with the ET rate, k_{ET}, is being given by

$$k_{ET} = k^{NA} / (1 + \kappa) \tag{II.12}$$

In the nonadiabatic limit ($\kappa \ll 1$), Eqn. II.12 reduces to the conventional result $k_{ET} = k^{NA}$, Eqn. II.6. In the medium-controlled limit ($\kappa \gg 1$), the maximal value for an ET rate corresponds to an activationless process ($E_a = 0$), being

$$k_{ET}^{MC} = \tau_s^{-1} (\lambda / 16\pi k_B T)^{1/2} \tag{II.13}$$

For $\lambda = 1000$ cm^{-1} and $T = 300$ K one obtains $k_{ET}^{MC} = 0.31/\tau_s$, which with $\tau_s = 200$ fs results in the medium-controlled activationless rate of $k_{ET}^{MC} = (700 \text{ fs})^{-1}$. Medium-controlled dynamic effects may be significant for the fastest process in the RC. The experimental observation of the ultrafast subpicosecond rate $k_2 = (900 \text{ fs})^{-1}$ [29], which is close to k_{ET}^{MC}, requires the incorporation of the effects of medium dynamics on charge separation in the RC.

II-C. Electronic, nuclear and dynamic parameters

The parameters which determine the nuclear Franck-Condon factors, Eqn. II.9 are free-energy gaps and the reorganization energies. These are:

(1) ΔG, the free-energy gap for the direct process k, which corresponds to the difference between the free energies of P*BH and of P^+BH^- at the equilibrium nuclear configurations. From the combination of experimental magnetic and phosphorescence data $-\Delta G = 2050 \pm 50$ cm^{-1} [35,36]. We take $-\Delta G = 2000$ cm^{-1}.

(2) λ, the recorganization energy for k. It was assumed that k is activationless with $\lambda \simeq \Delta G$ (within $\pm 25\%$) [15]. Recent computer simulations of interactions and molecular dynamics of the RC resulted in $\lambda = 1600$ cm^{-1} (within an uncertainty of ± 800 cm^{-1}) [37]. We shall take $\lambda = 2000$ cm^{-1}.

(3) $E_a = (\Delta G + \lambda)^2/4\lambda$ is the activation energy for k. In view of our choice of ΔG and λ, then $E_a = 0$.

(4) ΔG_1, the free-energy difference between ^{1}P*BH and P^+B^-H. Early attempts to estimate a lower limit for ΔG_1 from the temperature dependence of the exchange integral [39] for the P^+BH^- radical pair resulted in $\Delta G_1 \geqslant -250$ cm^{-1} [38]. However, more recent measurements have shown that the intrinsic accuracy of the previous data was overestimated [40]. From the combination of femtosecond time-resolved data [29] and the magnetic field dependence of the recombination dynamics of P^+BH^-, the limit $\Delta G_1 \geqslant -600$ cm^{-1} was inferred [40]. The value of ΔG_1 constitutes a central energetic parameter which dominates the mechanism of primary ET. In our model calculation we shall vary ΔG_1 over a broad range, taking $\Delta G_1 = -800$ cm^{-1} to $+600$ cm^{-1}.

(5) λ_1, the reorganization energy for k_1. No direct information is available, while computer simulations implied $\lambda_1 < \lambda$. We shall take $\lambda_1 = 1000$ cm^{-1}.

(6) ΔG_2, the energy gap for k_2 was taken as $\Delta G_2 = \Delta G - \Delta G_1$.

(7) λ_2, the reorganization energy for k_2, which in the absence of any information was taken is $\lambda_2 = \lambda_1$.

(8) The activation energies E_{a1} and E_{a2} for k_1 and k_2, respectively. As $-\Delta G_1 < \lambda_1$ the rate k_1 falls in the 'normal' Marcus regime and we take $E_{a1} = (\Delta G_1 + \lambda_1)^2/\lambda_1$. For k_2 we have $-\Delta G_2 > \lambda_2$ and the reaction corresponds to the inverted regime, where one expects reduction of the activation energy due to excitation of high-frequency intramolecular vibrational modes of the prosthetic group accompanying the ET. We shall take $E_{a2} = 0$.

The electronic terms are:

(9) The electronic couplings, V_{PB} and V_{BH}. These are taken to be related by $\alpha = V_{BH}/V_{PB} = 4$ from the recent intermolecular overlap calculations using the refined structure of *R. viridis* (Plato, M., personal communication). The superexchange interaction is given by Eqn. II.7. The vertical energy difference, δE, between the states P^+B^-H and P*BH, is given by

$$\delta E = \Delta G_1 + \lambda_1 \tag{II.13}$$

Finally, the relevant dynamic parameter is:

(10) The medium relaxation time, τ_s. In accord with the molecular dynamics simulations [34] we have varied τ_s over the range $\tau_s = 100$–300 fs. For large electronic coupling the adiabaticity parameter, Eqn. II.11, may become large, and solvent controlled effects, expressed by Eqn. II.12, become important. This may be the case for k_1, k_{-1} and k_2. We take k to be nonadiabatic and the other rates to be given by Eqn. II.12, which extrapolates smoothly between the nonadiabatic and the solvent-controlled limits.

II-D. Microscopic rate constants

The four ET rate constants are given by

$$k = \frac{2\pi}{\hbar}[1/4\pi\lambda k_B T]^{1/2}\left(\frac{V_{PB}V_{BH}}{\delta E}\right)^2 \exp\{-E_a/k_B T\} \tag{II.14}$$

$$k_1 = \frac{2\pi}{\hbar}[1/4\pi\lambda_1 k_B T]^{1/2}\frac{(V_{PB})^2}{\left(1+4\pi V_{PB}^2\tau_s/\hbar\lambda_1\right)}\exp\{-E_{a1}/k_B T\} \tag{II.15}$$

$$k_{-1} = k_1 \exp\{\Delta G_1/k_B T\} \tag{II.16}$$

$$k_2 = \frac{2\pi}{\hbar}[1/4\pi\lambda_2 k_B T]^{1/2}\frac{(V_{BH})^2}{(1+4\pi V_{BH}^2\tau_s/\hbar\lambda_2)}\exp\{-E_{a2}/k_B T\} \tag{II.17}$$

These rate constants, II.14–II.17, correspond to the classical limit which is realized when $k_B T \geqslant \hbar\omega_0$. Taking $\hbar\omega_0 = 80$–100 cm^{-1} [41] the classical limit prevails for $k_B T \geqslant 100$ K. The effects of coupling to high-frequency intramolecular vibrational modes of the prothetic groups, which cannot be handled within the classical limit, are not important in the normal region. Rates in the inverted region, i.e., k_2 are affected by weak coupling to high-frequency intramolecular vibrational modes [42], which cause the lowering of the activation energy. Therefore we take $E_{a_2} = 0$ in our calculations (see point (8) above). The numerical calculations were performed in the range $T = 300$–100 K.

III. Calculations

The kinetic scheme (Fig. 2) involves a proliferation of microscopic parameters. The analysis of the kinetic scheme was performed with the parameters discussed in subsection II-C. The nuclear, electronic and dynamic parameters are assumed to be temperature-independent.

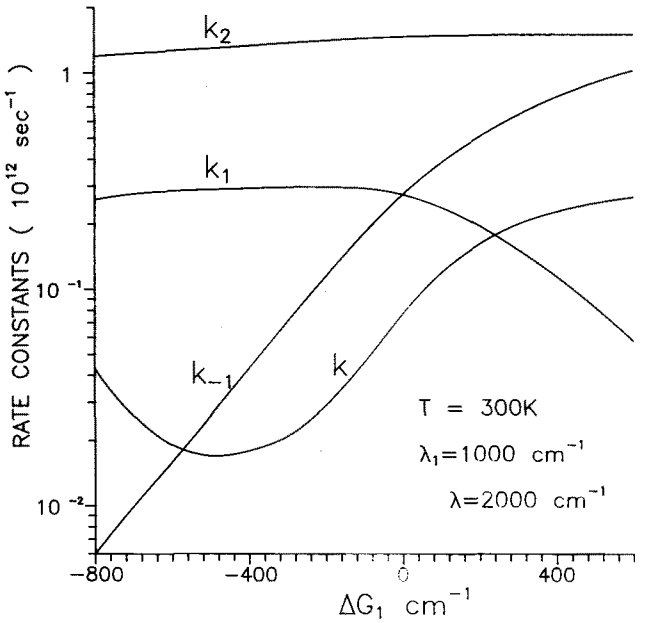

Fig. 3. The free-energy gap (ΔG_1) dependence of the elementary rate constants at 300 K.

The input parameters used in the calculation of the elementary rates were

$$\Delta G = -2000\ \mathrm{cm}^{-1}$$

$$\lambda = 2000\ \mathrm{cm}^{-1}$$

$$\lambda_1 = \lambda_2 = 1000\ \mathrm{cm}^{-1}$$

$$E_a = E_{a2} = 0$$

$$\tau_s = 100 - 300\ \mathrm{fs}$$

$$V_{BH}/V_{PB} = 4 \qquad \text{(III.1)}$$

The central energetic parameter, ΔG_1, which essentially determines the mechanism of the primary ET (sequential, superexchange or superposition of both) was varied over the broad range.

$$\Delta G_1 = -800\ \mathrm{cm}^{-1} \text{ to } +600\ \mathrm{cm}^{-1} \qquad \text{(III.2)}$$

The only missing parameter is now the electronic coupling, V_{PB}. This was determined by incorporating experimental kinetic information by demanding that the long effective relaxation time, $\tau_1 = (-s_-)^{-1}$, at room temperature should be equal to the experimental (rate determining) primary rate, i.e.,

$$(-s_-)^{-1} = 3.3 \cdot 10^{-12}\ \mathrm{s} \text{ at } 300\ \mathrm{K} \qquad \text{(III.3)}$$

Eqns. II.14–II.17 were used to calculate the elementary rates k, k_1, k_{-1} and k_2, which were then incorporated into Eqns. II.1–II.5 for the kinetic scheme, utilizing the parameters III.1 and III.2 together with the restriction III.2.

Once V_{PB} was fixed (for a given value of ΔG_1) at 300 K the same electronic couplings were used for the calculation of kinetic information at other temperatures. The output data involve:

(i) The elementary rate constants (Fig. 3);

(ii) The effective relaxation times τ_1 and τ_2;

(iii) The maximum concentration, B_{max}, of $[P^+B^-H]$, which appears at time t_{max};

(iv) The branching ratio F_{seq} for the sequential channel;

(v) The ratio of the slow to fast amplitudes in the decay of [P*BH].

All these attributes were calculated in the temperature range $T = 300$–100 K. The lowest temperature, $T = 100$ K, provides a reasonable description of the low-temperature kinetic data in the RC, as is evident from more detailed model calculations, using the full quantum mechanical expression for the ET rate [43].

IV. Results

We shall focus on the relevant observables, which can be confronted with experimental data. All the results of the kinetic modelling will be displayed versus the free-energy gap, ΔG_1, for several temperatures.

IV-A. Relaxation times

The room temperature (300 K) ET lifetimes $\tau_1 = 3.3 \cdot 10^{-12}$ s and τ_2 are portrayed in Fig. 4 in terms of the ratio τ_2/τ_1 for several values of τ_s. The variation of the lifetime ratio with τ_s is nearly parallel over the relevant range of ΔG_1. For each value of ΔG_1 the spread of the

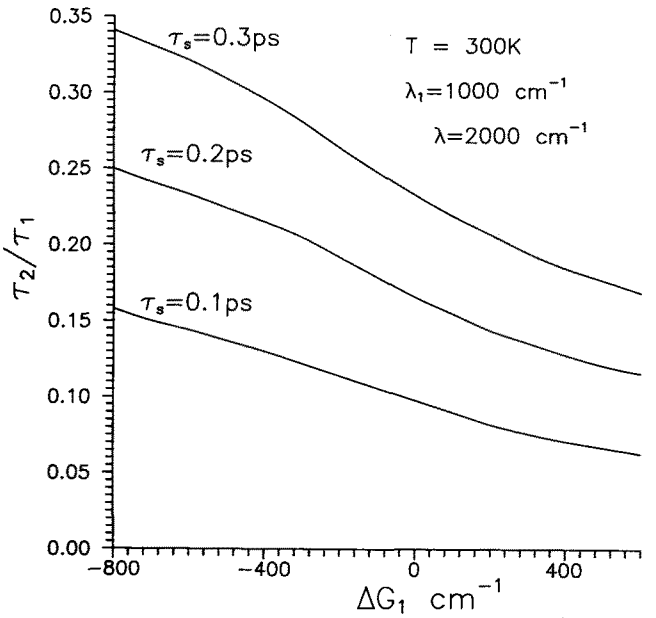

Fig. 4. The free-energy gap (ΔG_1) dependence of the ratio τ_1/τ_1 of the relaxation times for several values of τ at 300 K. For all these data $\tau_1 = 3.3$ ps.

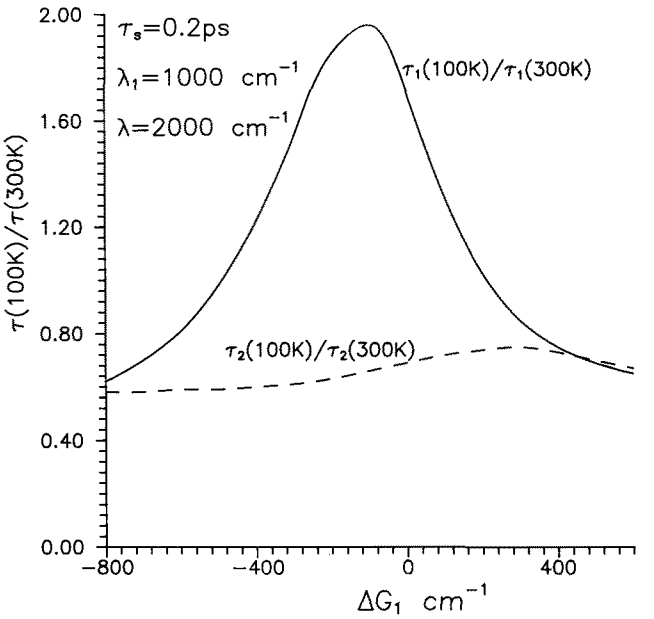

Fig. 5. The ΔG_1 dependence of the ratios τ_1(100 K)/τ_1(300 K) and τ_2(100 K)/τ_2(300 K), reflecting on the temperature dependence of the two relaxation times.

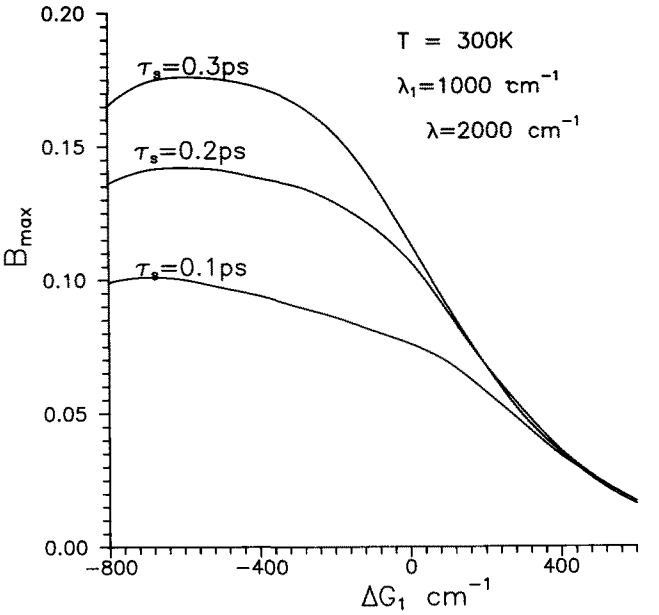

Fig. 6. The ΔG_1 dependence of the maximum concentration of the intermediate [P$^+$ B$^-$ H] at 300 K for several values of τ_s.

values of τ_2/τ_1 is about $\pm 40\%$ when τ_2 is varied from 100 fs to 300 fs. Utilizing the value of $\tau_s = 200$ fs from simulation data [34], we find τ_2/τ_1 to vary over the range 0.25–0.12 for $\Delta G_1 = -800$ cm^{-1} to $+600$ cm^{-1}. The temperature dependence of the relaxation times is presented in Fig. 5 in terms of the ratios τ_1(100 K)/τ_1(300 K) and τ_2(100 K)/τ_2(300 K). The lifetime τ_2 exhibits a very weak temperature dependence throughout the entire range of ΔG_1. The temperature dependence of τ_1 is rather weak. Reduction of the temperature from 300 K to 100 K results in a shortening of τ_1 by about 40% in the range $\Delta G_1 = -800$ cm^{-1} to -500 cm^{-1}, an increase of τ_1 up to a factor of 2 in the range $\Delta G_1 = -500$ cm^{-1} to -100 cm^{-1}, followed by the decrease of τ_1 in the range $\Delta G_1 = -100$ cm^{-1} to $+600$ cm^{-1}. The entire range of ΔG_1 corresponds to pseudoactivationless ET [43].

IV-B. The maximum concentration of [P$^+$B$^-$H] and the branching ratio

The values of B_{max} (Fig. 6) at 300 K reveal a moderate dependence on τ_s for low values of ΔG_1, while for $\Delta G_1 > 100$ cm^{-1} the dependence of B_{max} (at a fixed ΔG_1) on τ_s is weak. The model calculations reveal a nearly constant value of B_{max} over the range $\Delta G_1 = -800$ cm^{-1} to -100 cm^{-1} followed by a drop of B_{max} with increasing ΔG_1 at higher values (Fig. 6). The behavior of the branching ratio F_{seq} (Fig. 7) closely follows that of B_{max} (Fig. 8), revealing at 300 K at high value of F_{seq} for low values of $\Delta G_1 = -800$ cm^{-1} to -100 cm^{-1} and a gradual decrease of F_{seq} with increasing $\Delta G_1 > -100$ cm^{-1}. The temperature dependence of B_{max} (Fig. 8) and of F_{seq} (Fig. 7) reveal three regions:
Range (I): -800 cm$^{-1} \leqslant \Delta G_1 \leqslant -400$ cm^{-1}. A weak temperature dependence of B_{max} and F_{seq} is exhibited.
Range (II): 400 cm$^{-1} \leqslant \Delta G_1 \leqslant 0$. A transition region where the onset of a decrease of B_{max} and F_{seq} with decreasing temperature is exhibited.
Range (III): $\Delta G_1 \geqslant 0$. A strong temperature dependence of B_{max} and F_{seq}. The low temperature values of these observables being very low ($B_{max} < 0.02$ and $F_{seq} < 0.1$ at 100 K).

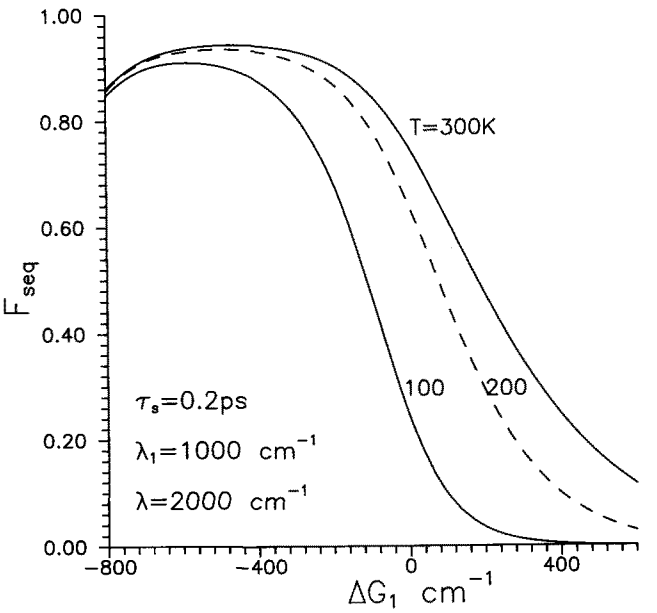

Fig. 7. The ΔG_1 dependence of the branching ratio F_{seq} between the sequential and superexcharge channels.

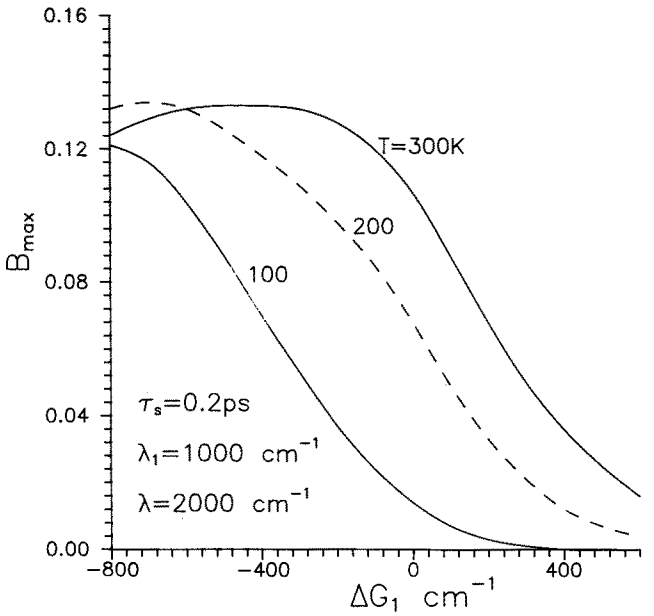

Fig. 8. The ΔG_1 and temperature dependence of B_{max}.

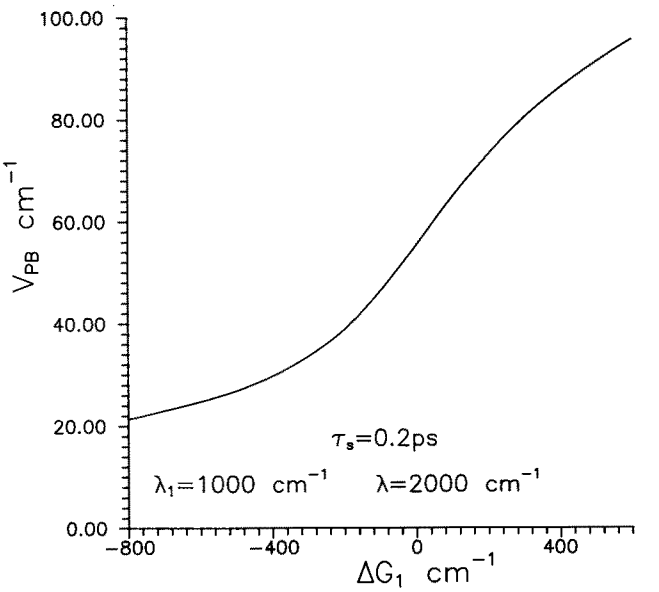

Fig. 10. The dependence of the electronic coupling $|V_{PB}|$ on ΔG_1, which is subject to the experimental constraint $\tau_1 = 3.3$ ps at 300 K.

IV-C. Amplitude ratio for the biexponential decay of $^1P^*BH$

The decay of $^1P^*$ is, in principle, nonexponential, being given according to Eqn. (A.6) by

$$A_+ \exp(-t/\tau_1) + A_- \exp(-t/\tau_1) \qquad \text{(IV.1)}$$

This behavior is due to the effect of the back-reaction, k_{-1}. In Fig. 9 we present the amplitude ratio A_+/A_- which is very large over the entire domain of ΔG_1. At 300 K the smallest value of the $A_+/A_- \simeq 15$ is exhibited in the range $\Delta G_1 = 0$ to 200 cm^{-1}, where the back-reaction k_{-1} is most efficient. This small deviation from nonexponentiality will require extremely high experimental accuracy at 300 K. At low temperatures (Fig. 9) this amplitude ratio is even larger, definitely precluding experimental observation.

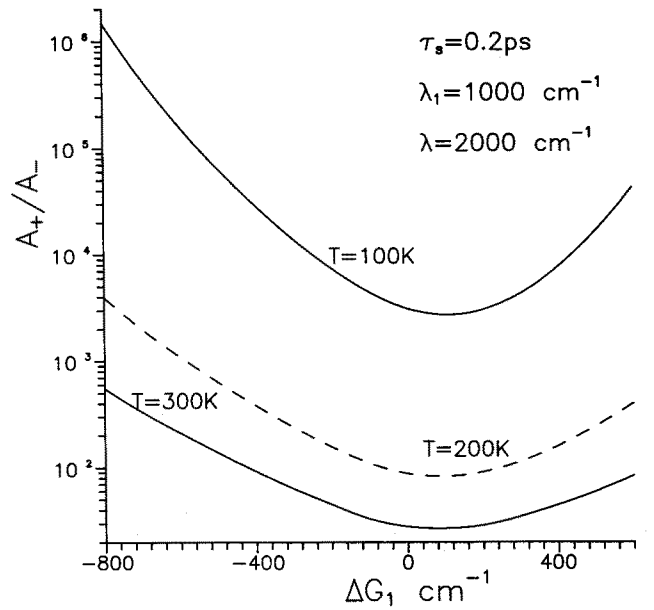

Fig. 9. The amplitude ratio A_+/A_- for the biexponential decay of $^1P^*BH$ at several temperatures.

IV-D. The electronic coupling

The dependence of $|V_{PB}|$ on ΔG_1, which satisfies the constraint (III.3) is presented in Fig. 10. The electronic coupling V_{BH} is related to these data by $|V_{BH}| = 4|V_{PB}|$. Both V_{PB} and V_{BH} increase with increasing ΔG_1. These electronic coupling terms are important for the elucidation of the magnetic interactions in the radical pair P^+BH^-, which will be considered in Section VI.

V. Direct kinetic information

V-A. Competition between sequential and superexchange mechanisms

From the foregoing results of the kinetic analysis extensive information emerged regarding the competition of the two-step sequential ET and the unistep superexchange mechanisms over a broad range of ΔG_1. Furthermore, the kinetic scheme implies that the relative contributions of the two parallel mechanisms are temperature-dependent. Accordingly, we can utilize the temperature dependence of the branching ratio, F_{seq} (subsection IV-B) for the classification of the mechanisms which are dominant in various energy domains. The dominance of a mechanism will be defined in an operational way when the branching ratio for that mechanism exceeds 80%. The following energy domains can be distinguished:

Range (I). Sequential mechanism at all temperatures. $\Delta G_1 \leqslant -400$ cm^{-1}. In this range F_{seq} is large (> 0.80) and $B_{max} = 0.15$–0.10 over the entire temperature domain. In this range the electronic coupling is relatively low $V_{PB} \simeq 20$–30 cm^{-1}.

Range (II). Superposition of sequential and superexchange mechanism at all temperatures. -400 cm$^{-1} \leqslant \Delta G_1 \leqslant 0$. At room temperature, $F_{seq} = 0.85$–0.75 with $B_{max} = 0.15$–0.12 at 300 K and $F_{seq} = 0.80$–0.20 with $B_{max} = 0.08$–0.02 at 100 K.

Range (III). Superposition of sequential and superexchange mechanisms at room temperature and superexchange mechanism at low temperature. $0 \leqslant \Delta G_1 \leqslant 400$ cm^{-1}. At room temperature, $F_{seq} = 0.80$–0.20 with $B_{max} = 0.12$–0.04, while at low temperature (100 K) $F_{seq} = 0.20$–0.02 with $B_{max} = 0.02$–0.05.

Range (IV). Superexchange mechanism at all temperatures. $\Delta G_1 \geqslant 400$ cm^{-1}. Here $F_{seq} < 0.20$ and $B_{max} < 0.025$ at all temperatures. In this range the electronic coupling is relatively high, $V_{PB} \geqslant 90$ cm^{-1}.

V-B. Experimental implications of kinetic analysis

The results of the kinetic analysis lead to the following conclusions:

(1) Two kinetic time constants. The experimental observation of biexponential time evolution with two time constants for the time-dependent absorption of P^+B^-H and of P^+BH^- is exhibited over a broad range of ΔG_1, which corresponds to ranges (I) and (II) over the entire temperature domain and for range (III) at room temperature. The necessary condition for the observation of this biexponential time evolution is a substantial, but not exclusive contribution of the sequential channel, so that the concentration of B (expressed in terms of B_{max}) is marked. The observation of biexponential decay at room temperature does not provide unambiguous evidence for the pure sequential mechanism.

(2) A single lifetime. The kinetics of the build-up of P^+BH^- can be characterized by a single time constant when the contribution of the superexchange channel is substantial. This state of affairs is realized for range (III) at low temperatures and in range (IV) over the entire temperature domain.

(3) Identification of the kinetic range. This can be accomplished on the basis of primary kinetic data by: (i) the identification of one or two decay lifetimes on the basis of detailed kinetic analysis; (ii) the magnitudes of B_{max} and F_{seq}; (iii) the temperature dependence of the general characteristics of the kinetics and of the observables.

V-C. Analysis of experimental data

The available direct kinetic data of Martin et al. on RCs of *Rb. sphaeroides* at room temperature [24], of Breton et al. at 10 K [26] and of Holzapfel et al. [29] at room temperature allow for a preliminary determination of the permissible free-energy ΔG_1 domain, where the results of our kinetic modelling are consistent.

(1) Two decay lifetimes. The experimental results [29] $\tau_2/\tau_1 = 0.26 \pm 0.10$ at 300 K are consistent with our model calculations for $\tau_s = 200$ fs (subsection IV-A and Fig. 4) over the range $\Delta G_1 = -800$ cm^{-1} to 200 cm^{-1}.

(2) The temperature dependence of τ_1. The experimental observation of the reduction of the primary ET rate constant with decreasing temperature is in qualitative agreement with the calculated results for τ_1(100 K)/τ_1(300 K) (Fig. 5) in the ranges $\Delta G_1 = -800$ to -500 cm^{-1} or 100 cm^{-1} to 400 cm^{-1}. A quantitative account of the experimental temperature dependence of the ET rate [44] requires the incorporation of thermal contraction of the RC upon cooling, which may result in the increase of the electronic coupling terms at low temperature. In view of the lack of information regarding thermal contraction effects of the protein medium of the RC, the experimental temperature dependence of τ_1 cannot be used for the determination of the permissible range of ΔG_1.

(3) The magnitude of B_{max}. Holzapfel et al. [29], have reported $B_{max} \simeq 0.15$ at 300 K. There seems to be a substantial uncertainty in the determination of B_{max}, which rests on limited experimental information regarding absorption coefficients of the prosthetic groups and their negative ions as well as of $^1P^*$. This rather uncertain room temperature result, $B_{max} \simeq 0.15$, is consistent with our model calculations (Fig. 6) over the range $\Delta G_1 = -800$ cm^{-1} to 100 cm^{-1}.

(4) The temperature dependence and general characteristics of the kinetics. The room temperature femtosecond spectroscopic data of Martin et al. [24] are consistent (within the large experimental uncertainty) with the existence of two lifetimes $\tau_1/\tau_2 > 5$, while the femtosecond spectroscopic data of Holzapfel et al. [29] seem to reveal two lifetimes with $\tau_1/\tau_2 = 4.0 \pm 1.5$ for *Rb. sphaeroides.* If these observations and analyses are borne out by subsequent work, one can conclude (see point (1)) that the primary process in *Rb. sphaeroides* corresponds to ranges (I) or (II) or (III), i.e., -800 cm$^{-1} \leqslant \Delta G_1 \leqslant 200$ cm^{-1}. A similar conclusion emerges from the analysis of the experimental absolute values of B_{max} within the present kinetic model (see point (3)). The lower limit of ΔG_1 can be somewhat reduced in view of the analysis of the energetics [40] which gives $\Delta G_1 \geqslant -600$ cm^{-1}. Thus, the permissible free energy domain which is consistent with the room-temperature kinetic data is -600 cm$^{-1} \leqslant \Delta G_1 \leqslant 200$ cm^{-1}. The low-temperature (10 K) femtosecond data for both *Rb. sphaeroides* and *R. viridis* were analyzed in terms of a single exponential decay of $^1P^*$ and buildup of P^+BH^-, which implies that the kinetics is either biexponential with $\tau_1 \approx \tau_2$ within experimental uncertainty, or that the

kinetics are characterized by a single lifetime. Provided that the occurrence of single-lifetime kinetics will be confirmed by further experiments, then the available low-temperature data seem to indicate that the primary kinetics correspond to ranges (III) or (IV). From the combination of the room-temperature results and the low-temperature data there is a distinct possibility that the primary mechanism falls within range (III), with $\Delta G_1 = -100$ to 200 cm^{-1} for *Rb. sphaeroides*. Thus, the primary mechanism may involve parallel sequential and superexchange at high temperature and essentially superexchange at low temperature. This conclusion is, of course, preliminary, requiring extensive further critical experimental scrutiny.

VI. Auxiliary information

Further information regarding the nature of the primary mechanism can be alluded from effects of external magnetic fields and from supplementary kinetic data for both wild-type and mutant RCs of *Rb. sphaeroides*. This auxiliary information bears on the energetics and the electronic coupling.

VI-A. Magnetic data

Magnetic interactions provide information on the properties of the P^+BH^- radical pair, i.e., its singlet-triplet splitting, J, and the triplet recombination rate. The small values of the singlet-triplet splitting in *Rb. sphaeroides* ($|J| \simeq (0.9 \pm 0.2) \cdot 10^{-3}$ cm^{-1}) [45], in *Rb. capsulatus* ($|J| \simeq (0.8 \pm 0.2) \cdot 10^{-3}$ cm^{-1}) [45] and in *Chloroflexus aurontiacus* ($|J| \simeq (1.90 \pm 0.5) \cdot 10^{-3}$ cm^{-1}) [45] point towards relatively small values of the electronic coupling terms provided that the configurational relaxation of the P^+BH^- radical pair is minor. It is of interest to combine the results of the present kinetic analysis with the theory of the magnetic effects [13,14], to provide some estimates for the ΔG_1 domain where the electronic coupling terms (Fig. 10) are consistent with the experimental value of J. The singlet-triplet splitting is

$$J = \delta E_S - \delta E_T \tag{VI.1}$$

where δE_S and δE_T are the energy shifts of the singlet and triplet states of P^+BH^-, respectively. As before, we shall limit the electronic contributions to the states $^1P^*$ and $^3P^*$ which contribute to δE_S [denoted $\delta E_S(^1P^*)$] and to δE_T denoted $\delta E_T(^3P^*)$, respectively.

A lower limit on the absolute value of the triplet shift was previously estimated [13] from the correlation between $\delta E_T(P^*)$ and the triplet-radical recombination rate k_T in terms of a model-independent result, which is invariant to the energetics of the P^+B^-H state and to the mechanism of the primary charge separation. We have obtained [13,14] from the experimental k_T rate $|\delta E_T(^3P^*)| \geqslant 2.5 \cdot 10^{-3}$ cm^{-1}, which will be used in subsequent analyses.

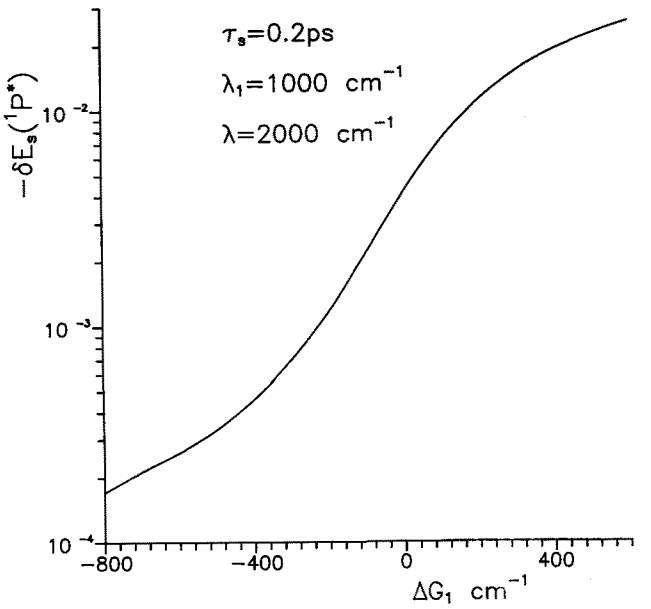

Fig. 11. The ΔG_1 dependence of the singlet shift of the P^+BH^- radical pair emerging from Eqn. V.2 together with the data of Fig. 10 and $V_{BH} = 4V_{PB}$.

In the evaluation of δE_S we neglect for the moment possible effects of configuration relaxation of P^+BH^- and assume that the electronic coupling terms V_{PB} and V_{BH} are independent of nuclear coordinates. Accordingly, the values of V_{PB} and $V_{BH} = 4V_{PB}$ (Fig. 10 and subsection IV-C) will be utilized for the evaluation of δE_S, which is given by [13,14]:

$$\delta E_S(^1P^*) = -\left[\frac{V_{BH}}{E_v(P^+B^-H) - E_v(P^+BH^-)}\right]^2 \times \left[\frac{V_{PB}^2}{E_v(^1P^*) - E_v(P^+BH^-)}\right] \tag{VI.2}$$

The vertical energies at the equilibrium configuration of the radical pair are $E_v(^1P^*) - E_v(P^+BH^-) = -\Delta G + \lambda$ where $\lambda = 2000$ cm^{-1}, together with $E_v(P^+B^-H) - E_v(P^+BH^-) = -\Delta G + \Delta G_1 + \lambda_1$ where $\Delta G = -2000$ cm^{-1} and $\lambda_1 = 1000$ cm^{-1}. The dependence of $\delta E_S(^1P^*)$ on ΔG_1 (Fig. 11) originates from the changes of the electronic coupling and from the weak energy dependence of the energy denominators. As is apparent from Fig. 11, $|\delta E_S(^1P^*)|$ is small in range (I) where $|\delta E_S| > 4 \cdot 10^{-4}$ cm^{-1}, increasing over range (II), where $|\delta E_S| = 4 \cdot 10^{-4}$–$4 \cdot 10^{-3}$ cm^{-1}, while for $\Delta G_1 = 100$ cm^{-1} $|\delta E_S| = 7 \cdot 10^{-3}$ cm^{-1}. We can conclude that, over the range $\Delta G_1 = -600$ cm^{-1} to 0, which is consistent with the room-temperature kinetic data (subsection V-B), $|\delta E_S|$ is smaller than or comparable to the experimental value of $|J|$. Over this region with $\delta E_S >$

$-4 \cdot 10^{-3}$ cm^{-1} and $|\delta E_T| \geq 2.5 \cdot 10^{-3}$ cm^{-1}, the resulting estimate of J is in accord with experiment. Possible effects of configurational relaxation of P^+BH^-, which may further modify the singlet shift [13], cannot be excluded.

VI-B. Mutagenic replacement of tyrosine M208

Experimental femtosecond kinetic data on mutagenetically altered RCs of *Rb. sphaeroides* are expected to infer on functional and structural importance of specific amino-acid residues. The exchange of the polar tyrosine M208 (Tyr) residue by the nonpolar phenylalanine (Phe) group in *Rb. sphaeroides* results in the slowing of the primary ET rate to $1/\tau_1^M = (25\ \text{ps})^{-1}$ [46], as compared with $1/\tau_1 = (3.5 \pm 0.4\ \text{ps})^{-1}$ for the native RC [29]. This observation can be rationalized in terms of the modification of the energetics of the P^+B^- ion pair state. According to recent energetic calculations [37] the replacement of Tyr M208, which is in van der Waals contact with both P and with B across the A branch, by Phe results in the increase of the energy of the P^+B^- state by approx. 1000 cm^{-1}. Such a change in the value of ΔG_1 has the following consequences: (i) The reduction of the nuclear Franck-Condon factor in k_1, resulting in the decrease of the rate-determining step in the sequential process. (ii) The increase of the vertical energy gap, δE, which will decrease V_{super}, Eqn. II.7, resulting in the decrease of the superexchange rate, k. Thus, both parallel channels will be retarded. To investigate the consequences of the energetic changes due to the Tyr M208 → Phe mutagenesis on ET kinetics, we have utilized the kinetic scheme of Section II and the nuclear parameters of Eqn. III.1 with the modification of the free-energy gap for k_1, which is taken as

$$\Delta G_1^M = \Delta G_1 + \delta G_1 \qquad \text{(VI.3)}$$

where $\delta G_1 = 1000$ cm^{-1} is the shift of the energy of P^+B^-. Assuming, for simplicity, that the mutant does not cause structural changes of the RC, the electronic couplings V_{PB} and V_{BH} were not varied and were taken as those for the native RC, being given by the data of Fig. 10. In Fig. 12 we present the lifetimes τ_1^M for the rate-determining ET step in this mutagenetically modified RC vs. the free-energy gap, ΔG_1, of the native system. These results reveal a marked lengthening of τ_1^M relative to τ_1 for the native RC, the room-temperature data ranging from $\tau_1^M/\tau_1 = 5$ for $\Delta G_1 = -600$ cm^{-1} to $\tau_1^M/\tau_1 = 8$ at $\Delta G_1 = 0$. These results for the permissible range of ΔG_1 are in accord with the experimental result $\tau_1^M/\tau_1 = 8$ at 300 K. Regarding the temperature dependence of τ_1^M, we expect that the sequential channel is thermally activated over a broad ΔG_1 range, while the superexchange channel is activationless. In ranges (I) and (II) τ_1^M exhibits quite a marked activated temperature dependence (Fig. 12), increasing with decreasing temperature, as appropriate for a marked contribution of the sequential channel. Finally, in range (III) the temperature dependence of τ_1^M is very weak, revealing a slight decrease of τ_1^M with decreasing temperature, as appropriate for a superexchange-dominated channel. The sorting out of the contribution of the superexchange channel at all temperatures sets in at lower values of ΔG_1 than for the native RC and that the contribution of the superexchange channel in the modified RC at low temperatures is dominant over the entire relevant range of ΔG_1. The present kinetic analysis of the ET kinetics in the mutagenetically modified RC has focused solely on the nuclear contribution to the ET rates and the energetic modification of the superexchange coupling, assuming that the individual electronic couplings V_{PB} and V_{BH} are invariant to the substitution of M208. Of course, even small configurational changes of the relative location of P and B across the A branch may modify V_{PB}.

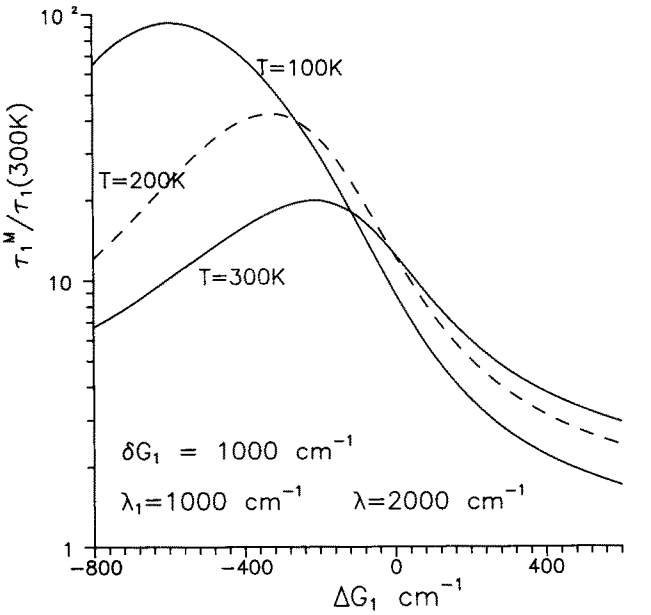

Fig. 12. The dependence of the lifetime τ_1^M of the rate-determining ET step in tyrosine M208 → phenylalanine mutagenetically modified RC, on the (free) energy gap ΔG_1 for the corresponding wild RC. Data are given for the temperature range $T = 300$ K–100 K.

VI-C. Unidirectionality of charge separation

The unidirectionality of the primary charge separation in the RC across the A branch constitutes a central dynamic phenomenon in photosynthesis. This effect was attributed to symmetry breaking [10,12], which may originate from the distinct electronic and nuclear contributions to the elementary ET rates, which in turn modify the experimental lifetimes.

(i) Modification of the electronic coupling terms V_{PB} and V_{BH} along the A and B branches [12]. Utilizing the

intermolecular overlap approximation these electronic coupling terms were computed for the atomic coordinates of *R. viridis* at a resolution of 2.6 Å. According to recent calculations based on the final refinement (2.2 Å) of the atomic coordinates of *R. viridis* RCs (Plato, M., private communication).

$$V_{PB}(A)/V_{PB}(B) = 2.0 \pm 0.4$$

$$V_{BH}(A)/V_{BH}(B) = 6.5 \pm 1.5$$

$$V_{BH}(B)/V_{PB}(B) = 1.1 \pm 0.2 \qquad \text{(VI.4)}$$

Thus the contributions of the electronic couplings to the sequential rate k_1 and the superexchange rate k are as follows:

$$\text{Electronic contribution to } k_1(A)/k_1(B) = |V_{PB}(A)/V_{PB}(B)|^2 = 4 \pm 1$$

$$\text{Electronic contribution to } k(A)/k(B)$$

$$= |V_{PP}(A)V_{BH}(A)/V_{PB}(B)V_{BH}(B)|^2 = 170 \pm 80.$$

(ii) Modification of the nuclear Franck-Condon factor. The microscopic environment of the B groups on the A and B branches of the RC is different with B_A located near the polar tyrosine M208 and B_B located near a nonpolar Phe. Energetic calculations for the RC have established that the energies of the ion pairs $P^+B_A^-$ and $P^+B_B^-$ are different with the latter being higher in energy [37]. The protein environment of the B branch of the RC where B_B is located near the Phe residue bears a close analogy to the A branch of the mutagenetically modified (Tyr M208 → Phe) RC, which was discussed in subsection VI-B. To obtain an estimate of the effects of unidirectionality on the parallel sequential superexchange mechanism we have performed again a kinetic simulation for ET across the B branch according to the scheme of Section II and nuclear parameters (III.1) together with the following modifications: (i) The electronic couplings $V_{PB}(B)$ and $V_{BH}(B)$ were scaled according to Eqn. (VI.4) with the data of Fig. 10 for $V_{PB}(A)$ and $V_{BH}(A) = 4V_{PB}(A)$. (ii) The free-energy gap between $^1P^*$ and P^+B^- across the B branch was modified to be taken according to Eqn. VI.3, i.e.,

$$\Delta G_1(B) = \Delta G_1(A) + 1000\ \text{cm}^{-1} \qquad \text{(VI.5)}$$

The lifetimes $\tau_1(A)$ and $\tau_1(B)$ were calculated neglecting crossing between the A and B branches. As $\tau_1(B)/\tau_1(A) > 1$, this assumption is a posteriori justified. In Fig. 13 we present the results for the ratio $\tau_1(B)/\tau_1(A)$ over the relevant range of $\Delta G_1(A)$, spanning the temperature domain $T = 300$–100 K. The total contribution to the unidirectionality can be separated to the nuclear term, δ_N, and electronic term, δ_e, so that

$$\frac{\tau_1(B)}{\tau_1(A)} = \delta_e \delta_N \qquad \text{(VI.6)}$$

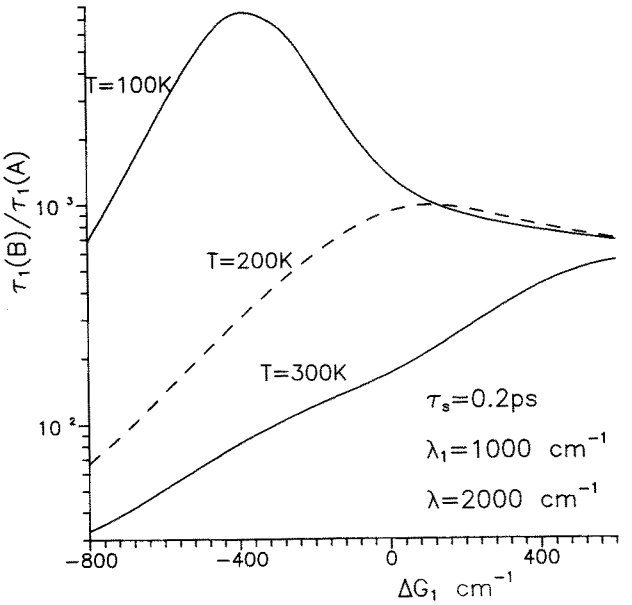

Fig. 13. Kinetic modelling of the unidirectionality of charge separation. The ratio $\tau_1(A)/\tau_1(B)$ of the rate-determining steps for ET across the A and B branches of the RC in the temperature range 300 K–100 K.

Both δ_N and δ_e contribute in the same direction, towards the enhancement of the lifetime ratio (Eqn. VI.6). The nuclear contribution is given by the lifetime ratio for the mutant which was calculated in subsection VI-B with the same energy gap as in Eqn. VI.5, so that $\delta_N = \tau_1^M/\tau_1$. The values of τ_1^M/τ_1 (Fig. 12) give δ_N at all temperatures. The electronic contribution δ_e is larger in the free-energy and the temperature domain, where the contribution of superexchange becomes dominant and thus the ratio $\tau_1(B)/\tau_1(A)$ increases at lower temperatures. The calculated value of $\tau_1(B)/\tau_1(A)$ over the permissible domain of ΔG_1 are 30–500 at room temperature (300 K) and 500–7000 at a low temperature (100 K). The lower experimental limit $\tau_1(B)/\tau_1(A) \geq 25$ at 90 K [47] is consistent with the results of these model calculations.

VII. Concluding remarks

The main conclusion emerging from our kinetic modelling is that the existing femtosecond kinetic data at high and low temperature are consistent with a primary charge separation model which involves the superposition of sequential and superexchange ET at room temperature and a superexchange mechanism at 10 K. In general, the explicit distinction between a superexchange and a sequential mechanism may be impossible, as both mechanisms can prevail in parallel over a broad range of the energetic, nuclear and electronic parameters. This kinetic scheme for the primary ET reduces to the limit of a nearly pure sequential mechanism for large negative ΔG_1 at all temperatures and to the limit

of almost pure superexchange mechanism for large positive ΔG_1 at all temperatures and for moderate ΔG_1 at low temperatures. Confronting theory with the available experimental data [29], we found that the recent experimental room-temperature femtosecond data are consistent with the results of our model calculations over a broad (free) energy domain of $-600\ \mathrm{cm}^{-1} \leqslant \Delta G_1 \leqslant 200\ \mathrm{cm}^{-1}$. The general features of the available low-temperature (10 K) data [26] raise the possibility that this (free) energy domain would be further narrowed to the range $-100\ \mathrm{cm}^{-1} \leqslant \Delta G_1 \leqslant 200\ \mathrm{cm}^{-1}$, whereupon the primary mechanism will involve parallel sequential-superexchange at high temperatures and the dominance of superexchange at low temperatures. In spite of the impressive current progress in femtosecond spectroscopy of RCs, these studies require very high sensitivity and accuracy, which demand experiments at the very front of the current 'state of the art' in this field. Further experimental data and their critical scrutiny will be of considerable importance.

The present analysis rests on three implicit assumptions. First, the temperature dependence of the nuclear, electronic and dynamic parameters has been disregarded. Second, we have asserted that configurational relaxation of the medium occurs on the subpicosecond time scale. Third, we have assumed that the protein medium is microscopically homogeneous.

Concerning the first assumption, we have attributed the temperature dependence of the ET kinetics solely to temperature effects on the nuclear Franck-Condon factors of the elementary rates k, k_1, k_{-1} and k_2, disregarding the temperature dependence of the free energy gaps, the reorganization energies, the electronic couplings and the medium relaxation time. Some justification for neglecting entropy contribution to the energy gaps was referred from a detailed analysis of the gap ΔG for k, where $\Delta G \simeq \Delta H$ [35]. Neglecting temperature effects on the electronic coupling terms V_{PB}, V_{BH} and V_{super} may be serious, as thermal contraction effects of the protein medium within the RC will increase the electronic couplings at lower temperatures, resulting in an additional decrease of τ_1 upon cooling. At present we can only conclude that the kinetic modelling, which predicts a weak temperature dependence of τ_1, is consistent with the non-Arrehnius weak temperature dependence at the negative apparent activation energy of the primary rate. A more refined treatment will require the incorporation of complex thermal contraction effects of the RC.

Regarding the second assumption pertaining to the relaxation dynamics of the protein medium we have assumed that the longitudinal relaxation time in the field of a fixed internal charge is $\tau_s \simeq 200$ fs, as inferred from molecular dynamics simulations [34]. We have further assumed that τ_s is temperature-independent. Accordingly, we have incorporated protein relaxation time, τ_s, into the theory of ET dynamics, treating the elementary rates in terms of Eqn. II.12, which is independent of τ_s for the nonadiabatic limit and reduces to the medium-controlled limit for $\kappa \geqslant 1$, according to Eqn. II.13. Sequential protein relaxation processes on a time-scale longer than τ_s were not considered, in view of our ignorance of the nature and consequences of such processes. Long-time relaxation processes provide a source of dynamics broadening of the relevant nuclear and electronic parameters.

The third assumption of microscopic homogeneity of the protein medium pertains to the disregard of static inhomogeneous broadening of the energetic, coupling and electronic parameters. Two classes of phenomena pertaining to such static inhomogeneous effects can be distinguished.

(1) Continuous inhomogeneous broadening. A continuous distribution of the energy gaps, of medium rearrangement energies and electronic coupling may originate from static disorder. Such kinetic phenomena are prevalent in proteins. An analogous continuous inhomogeneous broadening is exhibited in the optical absorption spectrum the P band in the RC, where hole-burning measurements [48,49] indicate that the P $\rightarrow {}^1\mathrm{P}^*$ electronic transition exhibits an inhomogeneous broadening of $\Delta \simeq 300\ \mathrm{cm}^{-1}$ for *Rb. sphaeroides* and of $\Delta \simeq 150\ \mathrm{cm}^{-1}$ for *Rp. viridis*. Although these values of Δ differ from the energetic spreads of the ion pair states, we can infer that a crude estimate for the energetic spread of $\mathrm{P}^+\mathrm{B}^-\mathrm{H}$ may be comparable to Δ; so that the inhomogeneous energetic spread, Δ_g, of ΔG_1 may be several hundreds of cm^{-1}. This inhomogeneous broadening of ΔG_1 is comparable to the energetic spread of each of the individual free-energy regions (I)–(IV), distinguished in subsection V-A. Accordingly, the assignment of a 'sharp' value of ΔG_1 is grossly oversimplified and the kinetic observables, e.g., τ_1, τ_2, B_{max} and F_{seq}, should be averaged over the domain of Δ_g.

(2) Structural heterogeneity of the RC. Several distinct microscopic structures of the RC may exist, in principle, and are characterized by different nuclear and electronic parameters. No structural evidence for such multimodal heterogeneity is available. Kinetic evidence regarding bimodal heterogeneity in RCs of *Chloroflexus aurantiacus* emerges from femtosecond time-resolved absorption data [49] which show that the decay of ${}^1\mathrm{P}^*$ is biexponential, characterized by two lifetimes of 2 ps and 8 ps at 240 K with an amplitude ratio of approx. 1. The lifetime of the short component and the amplitude ratio are temperature-independent. We have shown in subsection IV-C that the decay of ${}^1\mathrm{P}^*$ is biexponential, according to Eqn. V.5 with $A_+/A_- \geqslant 15$ at 300 K. The amplitude ratio estimated in subsection IV-C for the decay of ${}^1\mathrm{P}^*$ in a microscopically homogeneous RC provides a criterion for structural heterogeneity. Any observation of $A_+/A_- < 10$ at 300 K would imply

structural heterogeneity. Thus, the experimental value for the amplitude ratio $A_+/A_- \simeq 1$ in *Chloroflexus aurantiacus* [50] implies a structural heterogeneity with a bimodal distribution of the primary ET lifetimes.

The peaceful coexistence of the sequential and superexchange ET routes for the primary ET in the RC of some purple bacteria allows for the occurrence of efficient charge separation over a rather broad range of the energy gap ΔG_1 (and possibly of other nuclear and electronic parameters). In all these systems kinetic optimization is essential, with the primary process being sufficiently fast to compete with energy waste due to backtransfer to the antenna. What is required is an efficient primary process which is stable with respect to (moderate) variations of the energetic parameters. This energetic stability criterion is satisfied by the parallel sequential-superexchange mechanism, which constitutes an efficient and ultrafast charge separation over a rather broad energy range, ΔG_1, of approx. 800 cm^{-1} (2–3 kcal mol^{-1}). The occurrence of the parallel mechanism for the primary ET introduces an element of redundancy, which might be essential to ensure the prevalence of efficient primary charge separation in different photosynthetic RCs.

Acknowledgments

This research was supported by the Deutsche Forschungsgemeinschaft (Sonderforschungsbereich 143) at the Technische Universität München. The generous support of the Zelman Weinberg Research Fund for Chemical Physics at Tel-Aviv University is gratefully acknowledged.

Appendix

Analysis of primary kinetics

The basic kinetical scheme for the primary process that includes a superexchange channel (with rate constant k), and a sequential channel (with rate constants k_1 and k_{-1} for the direct and reverse first step, respectively, and k_2 for the second step) is given by:

$$\frac{d}{dt}[P^*BH] = -(k+k_1)[P^*BH] + k_{-1}[P^+B^-H]$$

$$\frac{d}{dt}[P^+B^-H] = k_1[P^*BH] - (k_{-1}+k_2)[P^+B^-H]$$

$$\frac{d}{dt}[P^+BH^-] = k[P^*BH] + k_2[P^+B^-H] \quad (A.1)$$

Eqns. A.1, with the initial conditions $[P^*BH](t=0) = 1$ and $[P^+B^-H](t=0) = [P^+BH^-](t=0) = 0$, are solved by the Laplace transform method. Denoting the Laplace transform of the three concentrations by:

$$\hat{A} = \int_0^\infty dt \exp(-st)[P^*BH]$$

$$\hat{B} = \int_0^\infty dt \exp(-st)[P^+B^-H]$$

$$\hat{C} = \int_0^\infty dt \exp(-st)[P^+BH^-] \quad (A.2)$$

one has

$$s\hat{A} - 1 = -(k+k_1)\hat{A} + k_{-1}\hat{B}$$

$$s\hat{B} = k_1\hat{A} - (k_{-1}+k_2)\hat{B}$$

$$s\hat{C} = k\hat{A} + k\hat{B} \quad (A.3)$$

from which one obtains:

$$\hat{A} = \left[s + k + k_1 - \frac{k_1 k_{-1}}{s + k_{-1} + k_2}\right]^{-1}$$

$$\hat{B} = k_2[(s+k+k_1)(s+k_{-1}+k_2) - k_1k_{-1}]^{-1} \quad (A.4)$$

In order to find the effective relaxation times one has to solve the quadratic equation

$$s^2 + s(k + k_1 + k_{-1} + k_2) + (k + k_1)(k_{-1} + k_2) - k_1k_{-1} = 0 \quad (A.5)$$

In terms of the two solutions, s_+ and s_-, one can write the time dependence of the various concentrations as:

$$[P^*BH](t) = \frac{s_+ + k_{-1} + k_2}{s_+ - s_-}\exp\{s_+t\} - \frac{s_- + k_{-1} + k_2}{s_+ - s_-}\exp\{s_-t\}$$

$$[P^+B^-H](t) = \frac{k_1}{s_+ - s_-}[\exp\{s_+t\} - \exp\{s_-t\}]$$

$$[P^+BH^-](t) = 1 + \frac{k(s_+ + k_{-1} + k_2) + k_1k_2}{s_+(s_+ - s_-)}\exp\{s_+t\}$$

$$- \frac{k(s_- + k_{-1} + k_2) + k_1k_2}{s_-(s_+ - s_-)}\exp\{s_-t\} \quad (A.6)$$

References

1 Deisenhofer, J. and Michel, H. (1989) EMBO J. 8, 2149–2170.
2 Komiya, H., Yeates, T.O., Rees, D.C., Allen, J.P. and Feher, G. (1988) Proc. Natl. Acad. Sci. USA 85, 9012–9016.
3 Budil, D.E., Gast, P., Chang, C.-H., Schiffer, M. and Norris, J.R. (1987) Annu. Rev. Phys. Chem. 38, 561–583.
4 Woodbury, N.W., Becker, M., Middendorf, D. and Parson, W.W. (1985) Biochemistry 24, 7516–7521.
5 Fischer, S.F., Nussbaum, I. and Scherer, P.O.J. (1985) in Antennas and Reaction Centers of Photosynthetic Bacteria (Michel-Beyerle, M.E., ed.), pp. 256–263, Springer, Berlin.
6 Jortner, J. and Michel-Beyerle, M.E. (1985) in Antennas and Reaction Centers of Photosynthetic Bacteria (Michel-Beyerle, M.E., ed.), pp. 345–365, Springer. Berlin.

7 Jortner, J. and Bixon, M. (1987) in Protein Structure Molecular and Electronic Reactivity (Austin, R., Buhks, E., Chance, B., DeVault, D., Dutton, P.L., Frauenfelder, H. and Gol'danskii, V.I., eds.), pp. 277–308, Springer, New York.
8 Ogrodnik, A., Remy-Richter, N., Michel-Beyerle, M.E. and Feick, R. (1987) Chem. Phys. Lett. 135, 576–581.
9 Norris, J.R., Budil, D.E., Tiede, D.M., Tang, J., Kolaczkowski, S.V., Chang, C.H. and Schiffer, M. (1987) in Progress in Photosynthetic Research (Biggens, J., ed.), Vol. I, pp. 1.4.363–1.4.369, Martinus Nijhoff, Dordrecht.
10 Michel-Beyerle, M.E., Plato, M., Deisenhofer, J., Michel, H., Bixon, M. and Jortner, J. (1988) Biochim. Biophys. acta 932, 52–70.
11 Bixon, M., Jortner, J., Plato, M. and Michel-Beyerle, M.E. (1988) in The Photosynthetic Bacterial Reaction Center. Structure and Dynamics (Breton, J. and Vermeglio, A., eds.), pp. 399–420, NATO ASI Series, Plenum, New York.
12 Plato, M., Möbius, K., Michel-Beyerle, M.E., Bixon, M. and Jortner, J. (1988) J. Am. Chem. Soc. 110, 7279–9285.
13 Michel-Beyerle, M.E., Bixon, M. and Jortner, J. (1988) Chem. Phys. Lett. 151, 188–194.
14 Bixon, M., Michel-Beyerle, M.E. and Jortner, J. (1988) Isr. J. Chem. 28, 155–168.
15 Bixon, M., Jortner, J., Michel-Beyerle, M.E. and Ogrodnik, A. (1989) Biochim. Biophys. Acta 977, 273–286.
16 Friesner, R.A. and Won, Y. (1989) Biochim. Biophys. Acta 977, 99–122.
17 Marcus, R.A. (1988) Isr. J. Chem. 28, 205–213.
18 Haberkorn, R., Michel-Beyerle, M.E. and Marcus, R.A. (1979) Proc. Natl. Acad. Sci. USA 70, 4185–4188.
19 Marcus, R.A. (1987) Chem. Phys. Lett. 133, 471–477.
20 Chekalin, S.V., Matveetz, Ya.A., Shkuropatov, A.Ya., Shuvalov, V.A. and Yartzev, A.P. (1987) FEBS Lett. 216, 245–248.
21 Fischer, S.F. and Scherer, P.O.J. (1987) Chem. Phys. 115, 151–158.
22 Marcus, R.A. (1988) Chem. Phys. Lett. 146, 13–22.
23 Creighton, S., Hwang, J.-K., Warshel, A., Parson, W.W. and Norris, J. (1988) Biochem. 27, 774–781.
24 Martin, J.-L., Breton, J., Hoff, A.J., Migus, A. and Antonetti, A. (1986) Proc. Natl. Acad. Sci. USA 83, 957–961.
25 Breton, J., Martin, J.-L., Migus, A., Antonetti, A. and Orszag, A. (1986) Proc. Natl. Acad. Sci. USA 83, 5121–5125.
26 Breton, J., Martin, J.-L., Fleming, G.R. and Lambry, J.-C. (1988) Biochemistry 27, 8276–7284.
27 Lockhart, D.J., Goldstein, R.F. and Boxer, S.G. (1988) J. Chem. Phys. 89, 1408–1415.
28 Ogrodnik, A., Eberl, U., Heckmann, R., Kappl, M., Feick, R. and Michel-Beyerle, M.E. (1991) J. Phys. Chem., in press.
29 Holzapfel, W., Finkele, U., Kaiser, W., Oesterhelt, D., Scheer, H., Stilz, H.U. and Zinth, W. (1989) Chem. Phys. Lett. 160, 1–7.
30 Kirmaier, C. and Holten, D. (1990) Proc. Natl. Acad. Sci. USA 87, 3552–3556.
31 Jortner, J. (1976) J. Chem. Phys. 64, 4860–4867.
32 Marcus, R.A. (1956) J. Chem. Phys. 24, 966–978 and 979–989.
33 Rips, I. and Jortner, J. (1987) J. Chem. Phys. 87, 2090–2099.
34 Treutlein, H., Schulten, K., Deisenhofer, J., Michel, H., Brunger, A. and Karplus, M. (1988) The Photosynthetic Bacterial Reaction Center. Structure and Dynamics (Breton, J. and Vermeglio, A., eds.), NATO ASI Series A 149, 139–150, Plenum Press, New York.
35 Ogrodnik, A., Volk, M., Letterer, R., Feick, R. and Michel-Beyerle, M.E. (1988) Biochim. Biophys. Acta 936, 361–371.
36 Goldstein, R.A., Takiff, L. and Boxer, S.G. (1988) Biochim. Biophys. Acta 934, 253–263.
37 Parson, W.W., Chu, Z.-T. and Warshel, A. (1990) Biochim. Biophys. Acta, in press.
38 Bixon, M., Jortner, J., Michel-Beyerle, M.E., Ogrodnik, A. and Lersch, W. (1987) Chem. Phys. Lett. 140, 626–630.
39 Moehl, K.W., Lous, E.J. and Hoff, A.J. (1987) Chem. Phys. Lett. 121, 22–27.
40 Michel-Beyerle, M.E. and Ogrodnik, A. (1990) in Progress in Photosynthetic Research (Baltscheffsky, M., ed.), Martinus Nijhoff, Dordrecht, in press.
41 Bixon, M. and Jortner, J. (1986) J. Phys. Chem. 90, 3795–3800.
42 Bixon, M. and Jortner, J. (1991) J. Phys. Chem., in press.
43 Bixon, M. and Jorter, J. (1989) Chem. Phys. Lett. 159, 17–20.
44 Fleming, G.R., Martin, J.L. and Breton, J. (1988) Nature 333, 190–192.
45 Lersch, W., Lang, E., Feick, R., Coleman, W.J., Youvan, D.C. and Michel-Beyerle, M.E. (1989) Perspective in Photosynthesis (Jortner, J. and Pullman, B., eds.), pp. 81–90, Kluwer, Dordrecht.
46 Zinth, W., Holzapfel, W., Finkele, U., Kaiser, W., Oesterhelt, D., Scheer, H., Stilz, H.U. (1990) in Progress in Photosynthetic Research (Baltscheffsky, M., ed.), Martinus Nijhoff, Dordrecht, in press.
47 Aumeier, W., Eberl, U., Ogrodnik, A., Volk, M., Shiedel, G., Feick, R., Plato, M. and Michel-Beyerle, M.E. (1990) in Progress in Photosynthetic Research (Baltscheffsky, M., ed.), Martinus Nijhoff, Dordrecht, in press.
48 Hayes, J.M., Gillie, J.K., Tang, D. and Small, G.J. (1988) Biochim. Biophys. Acta 932, 287–305.
49 Boxer, S.G., Lockhart, D.J. and Middendorf, T.R. (1986) Chem. Phys. Lett. 123, 476–482.
50 Martin, J.-L., Breton, J., Lembry, G.C., Feick, R., Michel-Beyerle, M.E., Robles, S. and Youvan, D. (1990) in Ultrafast Phenomena Meeting, May 14–17, 1990, Monterey, CA.